ELSEVIER

Contents lists available at ScienceDirect

Chemical Geology

journal homepage: www.elsevier.com/locate/chemgeo





High mercury enrichments in sediments from the Baltic continent across the late Cambrian: Controls and implications

Leibo Bian ^a, Anthony Chappaz ^b, Niels Hemmingsen Schovsbo ^c, Arne Thorshøj Nielsen ^d, Hamed Sanei ^{a,*}

- ^a Lithospheric Organic Carbon (L.O.C) Group, Department of Geoscience, Aarhus University, Aarhus, Denmark
- b STARLAB, Department of Earth and Atmospheric Sciences, Central Michigan University, Brooks Hall 314, Mount Pleasant, MI 48859, USA
- Department of Reservoir Geology, Geological Survey of Denmark and Greenland, Copenhagen, Denmark
- d Department of Geosciences and Natural Resource Management, University of Copenhagen, Copenhagen, Denmark

ARTICLE INFO

Editor: Michael E. Boettcher

Keywords: High mercury enrichment Reducing conditions Volcanic activities Alum Shale Late Cambrian

ABSTRACT

The late Cambrian witnessed significant biological and environmental changes. However, the main triggers responsible for that formidable turnover remain largely unknown. This study investigates mercury (Hg) enrichments from the late Miaolingian to Furongian section in a unique Alum Shale drilled core obtained from southeast Sweden. Our results show that the background level of Hg is relatively high because of the presence of reducing conditions and continuous Hg supply from water mass. However, our most spectacular findings are the presence of four Hg anomalies. The most pronounced Hg anomalies are characterized by the high values in total Hg (\sim 900 ppb) and Hg/TOC ratio (\sim 80), as well as specific signatures of mass independent fractionation of Hg (MIFs; Δ^{199} Hg, Δ^{201} Hg, and Δ^{200} Hg) that we attribute to volcanic-derived Hg. This Hg loading event occurred immediately after the globally recognized Steptoean Positive Carbon Isotope Excursion (SPICE) event and could be attributed to volcanic activities during that period.

1. Introduction

The late Cambrian interval (500–487 Ma) is a remarkable period in Earth's history, because it was associated with loss of around 50% of global species and a one-fold increase in proportion of extinct genera (Saltzman et al., 2015; Fan et al., 2020). Previous examinations of sedimentary records highlight profound environmental variations such as atmospheric oxygenation, widespread anoxia, carbon and sulfur isotope excursions, regional water mass warming, and polar wander events, potentially induced by significant tectonic activity (Elrick et al., 2011; Gill et al., 2011; Saltzman et al., 2011; Schiffbauer et al., 2017; Jiao et al., 2018). Physical, chemical and biological triggers such as widespread oceanic anoxia, mass extinction, and volcanic activity usually occurred through Earth's history (Shen et al., 2019a; Bauer et al., 2021; Schoepfer et al., 2022). Mass extinction and oceanic anoxia phenomena were both investigated thoroughly during the late Cambrian (Saltzman et al., 2000, 2015; Gill et al., 2011, 2021; Fan et al., 2020). However, the effect of synchronous volcanic activity in sedimentary archives has not been examined to date, which may limit the understanding on atmospheric-oceanic-biological nexus during the late

Mercury (Hg) anomalies are defined as significantly higher concentrations of Hg (and/or Hg/TOC ratio) compared to the natural background (e.g., Sanei et al., 2012). They can be used as a proxy for identifying ancient volcanic activity in sedimentary records (Grasby et al., 2019). Prior to the Anthropocene, major sources of Hg emission were volcanic eruptions and degassing (Pyle and Mather, 2003; Percival et al., 2021). Given its short residence time in the environment, any anomalous rise of Hg in the geological record is attributed to a significant and prolonged change of the regular Hg flux reaching the sedimentwater interface (Mason and Sheu, 2002; Selin, 2009; Outridge et al., 2018). Mercury anomalies are associated with the first-order "big five" major mass extinction events and sub-order bio-extinction events as well as several oceanic anoxic events (Sanei et al., 2012; Sial et al., 2013; Thibodeau et al., 2016; Jones et al., 2017; Racki et al., 2018; Shen et al., 2019a, 2022). These observations led to the hypothesis that these major extinction events were linked to or possibly triggered by intense volcanic activity.

E-mail address: sanei@geo.au.dk (H. Sanei).

^{*} Corresponding author.

Chemical Geology 599 (2022) 120846

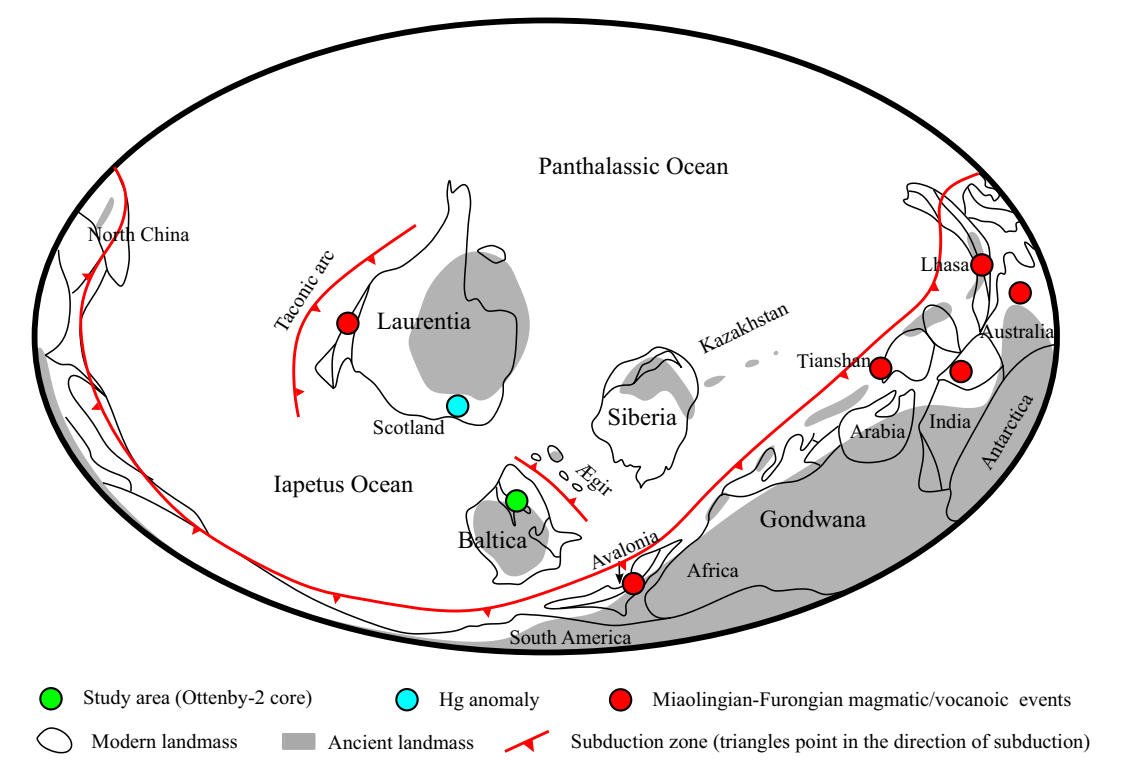


Fig. 1. Paleo-reconstruction of the later Cambrian Earth, modified from Scotese (2001). Hg anomaly is from Pruss et al. (2019). Locations and datings of the later Cambrian volcanic events are supplied in Table 2.

Today, the predominant species of Hg in the atmosphere is Hg(0) (~90%) (Fitzgerald et al., 2007). Mercury (0) can be oxidized into Hg(II) species and deposited through wet and dry deposition or via direct incorporation in plants and soils, where it is subsequently oxidized to Hg (II) (Outridge et al., 2018). Mercury has seven stable isotopes (196 Hg, 198 Hg, 199 Hg, 200 Hg, 201 Hg, 202 Hg, and 204 Hg) that are fractionated in the environment by both mass-dependent (Hg-MDF, denoted as δ^{202} Hg) and mass-independent (Hg-MIF, denoted as Δ^{199} Hg, Δ^{200} Hg, Δ^{201} Hg, and Δ^{204} Hg) processes. Mercury isotopes have been proven to be useful tracers (1) to disentangle between Hg(II) and Hg(0) deposition (Obrist et al., 2017), (2) to identify sources and processes involving Hg across Earth's history (Thibodeau et al., 2016; Zerkle et al., 2021), and (3) to provide new insights on Hg atmospheric (photo)chemistry (Chen et al., 2012; Zerkle et al., 2020). Mercury mass-dependent fractionation (MDF) occurs during geochemical reactions driven by kinetic and equilibrium exchanges such as methylation and adsorption processes (Lepak et al., 2020), and is typically denoted as δ^{202} Hg. Mass independent fractionations (MIFs) usually indicate that Hg underwent photochemical reactions that do not depend on mass (Tsui et al., 2020), and are mostly associated with odd isotopes (i.e., Δ^{199} Hg and Δ^{201} Hg) and result from the byproduct of photochemical demethylation (in biota) and photochemical reduction in sediments (Blum et al., 2014). However, less prominent MIF mechanisms have been characterized with even isotopes (even-MIFs) that are thought to be the result of nuclear self-shielding (Mead et al., 2013), and are denoted as Δ^{200} Hg and Δ^{204} Hg. Magnetic isotope effect (MIE) induces the largest mass-independent Hg isotope fractionation (MIF) of odd Hg isotopes during the reduction of Hg (II) in presence of light and water (Janssen et al., 2016) while nuclear volume effect (NVE) leads to relatively small Hg-MIF fractionation (Bergquist and Blum, 2007). Odd Hg-MIFs are particularly useful to track sources and Hg transformations (Tsui et al., 2020). In oceanic systems, odd Hg-MIF are robust to post-depositional alteration (Grasby et al., 2017) and can record additional, complementary atmospheric constraints (Zerkle et al., 2020). During the late Cambrian, vegetation cover and soil development were minimal, supporting a model where volcanic Hg(0)

would have been the crucial source of Hg to the atmosphere (Grasby et al., 2019). Mercury released from volcanoes is mostly characterized by near-zero odd and even Hg-MIF signatures (Zambardi et al., 2009; Blum et al., 2014; Zerkle et al., 2020; Edwards et al., 2021).

The lower Paleozoic, organic matter-rich Alum Shale is widely distributed in northwestern Europe and well-studied in paleogeography (Nielsen and Schovsbo, 2015), providing an ideal example to investigate Hg systems during the late Cambrian. The late Cambrian environmental and biological variations have been documented for a long time (e.g., Gill et al., 2011; Saltzman et al., 2015). However, the effects of late Cambrian volcanic activity interpreted by Hg anomaly have been largely ignored. This study aims to fill this gap and our goals were to (1) determine the late Cambrian Hg variations in the Alum Shale, (2) identify controls that contributed to Hg enrichments within this shale, and (3) discuss potential environmental and biological implications.

2. Geological setting

The lower Paleozoic Alum Shale, deposited in the western margin of the Baltic continent, covers an approximate area of 100, 000 km² in northwestern Europe (Fig. 1). This shale is highly enriched in organic matter (up to 28.0 wt%; Sanei et al., 2014) and redox metals (e.g., up to 6000 ppm V; Schovsbo, 2001). The deposition of this shale straddles the Miaolingian, Furongian, and Early Ordovician (Tremadocian) (Nielsen and Schovsbo, 2015). The long and stable stratigraphic connection and high-resolution fossils record within this shale contribute to a well-examined stratigraphy and geography (Nielsen and Schovsbo, 2006; Nielsen and Ahlberg, 2019). During the deposition of the Alum Shale, the water connection between the Baltoscandian Basin and the Iapetus Ocean was suggested to be persistent (Sturesson et al., 2005; Gill et al., 2021).

The studied Ottenby-2 core was drilled in southern Öland, Sweden (GPS Coordinates: 56.14741 N, 16.244316 E). The detailed trilobite/graptolite biostratigraphy of this core was described in Bian et al. (2021). The Alum Shale at this site was deposited under a relatively

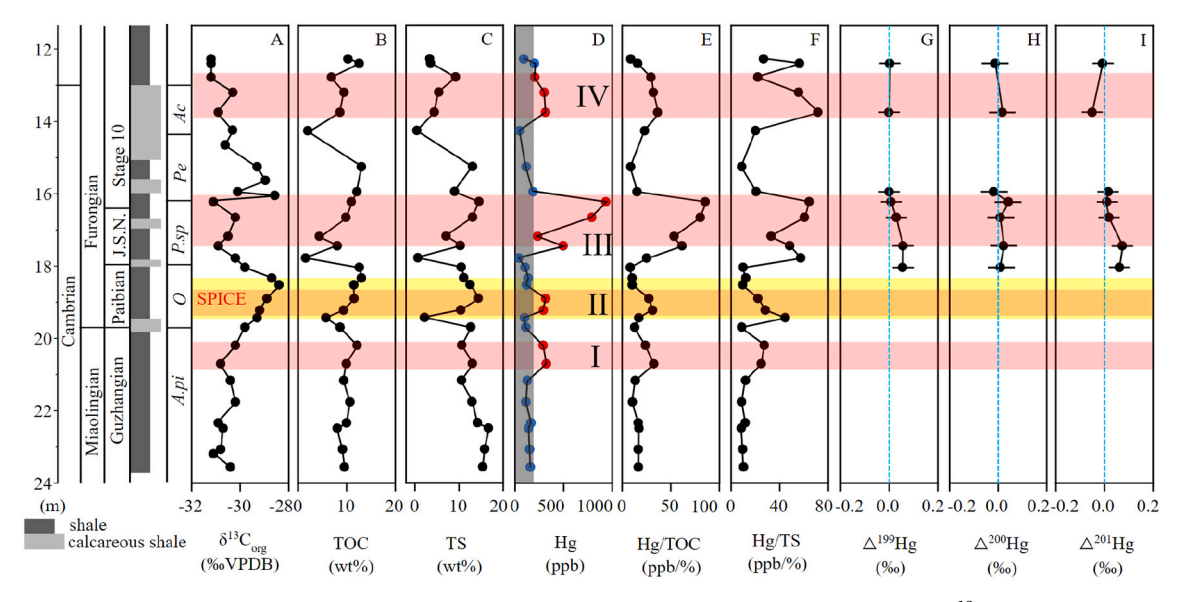


Fig. 2. Geochemical profiles of Ottenby-2 core in the late Cambrian, Alum Shale of Scandinavia. (A) organic carbon isotope ($\delta^{13}C_{org}$), (B) total organic carbon (TOC), (C) total sulfur (TS), (D) mercury (Hg), (E) Hg/TOC, (F) Hg/TS, (G) \triangle^{199} Hg, (H) \triangle^{200} Hg, and (I) \triangle^{201} Hg for the Alum Shale along with lithology. Zones I to IV marked by light red color represent four major mercury anomalies. Yellow zone marks the Steptoean Positive Carbon Isotope Excursion (SPICE) event. In biostratigraphic profile, from bottom to top, A.pi: *Agnostus pisiformis*, O: *Olenus*, P.sp.: *Parabolina spinulosa*, Pe: *Peltura*, and Ac: *Acerocare* (Bian et al., 2021). In panel D, red points represent volcanic Hg input, while blue circles mean basic Hg enrichment influenced by redox condition changes. In panel G-H, the horizontal bars of the isotope indicate standard deviation values (2 s.d.) of Hg isotopes. Source data is provided in Table 1. (For interpretation of the references to color in this figure legend, the reader is referred to the web version of this article.)

shallow water condition and the redox condition remained reducing (Nielsen and Schovsbo, 2015; Bian et al., 2021). The lithology of this core is mainly composed of carbonate-poor shale and subordinate calcareous shale. The biostratigraphic record in conjunction with organic carbon isotope suggests that the core straddles the Miaolingian and Furongian Series. Stratigraphically, this core contains the upper Miaolingian to lower Furongian succession and then a nearly continuous, condensed middle to upper Furongian succession. The chronostratigraphic boundaries of this core are calibrated by Olenus ssp. and Acerocare ssp. for the base and top of Furongian, respectively. The Olenus Superzone and organic carbon isotope excursion were used to constrain the globally recognized Steptoean Positive Carbon Isotope Excursion (SPICE) event (Fig. 2; Saltzman et al., 2000; Zhao et al., 2022). The thermal maturity of this core was examined by organic geochemical and petrographic methods, showing that the samples are immaturemarginally mature (Petersen et al., 2013).

3. Methods

About 3 g samples were pulverized using a corundum mortar, homogenized, and separated into different aliquots for total organic carbon (TOC), elemental, and isotopic analyses. All powdered samples were sieved through a non-metal, 74- μ m sieve at Aarhus University. TOC contents and Mo concentrations are compiled from Bian et al. (2021). TOC contents were measured using the Hawk pyrolysis systems (Wildcat Technologies, USA). Data quality was checked by replicates and was better than 5%. Molybdenum concentrations were analyzed through the Inductively Coupled Plasma Mass Spectrometry (ICP-MS) at the ACME Lab, Vancouver. Data precision was examined by reference (OREAS 45-E), replicates (\pm 2%), and blanks.

3.1. Total sulfur

Total sulfur (TS) contents were measured through the CS 200 analyzer at the Geological Survey of Denmark and Greenland. Approximate 0.05 g samples were treated with 2 M HCl solution at 65 $^{\circ}$ C for 2 h, followed by drying samples at room temperature for 24 h prior to

analysis. Data quality was checked by replicates (\pm 5%).

3.2. Organic carbon isotopes

Organic carbon isotopes were measured by the mass spectrometer (ThermoFinnigan MAT 253 Plus) at Northwest University. Approximate 1 g powdered samples were acidified with 6 N HCl for 24 h to remove calcareous parts, and were then buffered to a neutral pH, filtered, and dried at 75 °C. The residues were weighted into tin capsules, combusted at 950 °C in an Elemental Analyzer to generate CO₂ that was then transferred to the isotope mass spectrometer for measuring carbon isotopes. Organic carbon isotopes are expressed in delta notation $(\delta^{13}C_{org})$ in per mil. The final $\delta^{13}C_{org}$ values are relative to the Vienna Pee Dee Belemnite (V-PDB) standard to characterize the isotopic compositions. Analytical precision was better than 0.3‰.

3.3. Mercury concentration and isotopes

Mercury concentration analyses were performed through a DMA-80 automatic Hg analyzer (Milestone, Italy) and Hg isotopes were measured by a Cold Vapor-Multicollector Inductively Coupled Plasms Mass Spectrometry (CV-MC-ICPMS, Nu Instruments, U.K.) at State Key Laboratory of Environmental Geochemistry, Chinese Academy of Sciences.

For analyses of Hg contents, the powdered samples were decomposed in the combustion tube to remove interfering impurities, and subsequently, the purified gas was transported to the amalgamator, where Hg vapor was amalgamated with gold and heated for subsequent detection through an atomic absorption spectrometer. Data accuracy and precision were assessed by reference material (GBW07405) and duplicates (within $\pm 5\%$). The standard samples gave an average Hg concentration of 291 ± 22.5 ppb (2 s.d., n=20) that is consistent with standard value (290 \pm 30 ppb). The final Hg concentrations documented are the average value of the duplicate tests.

Based on the measured Hg concentrations, ~ 0.5 g samples were added into 10 mL of 40% mixed acid solution (HNO₃/HCl = 3:1, ν/ν) and then were analyzed using a combustion-trapping method developed for Hg isotopes analysis (Sun et al., 2013). After that, the Hg-trapping

Table 1Analytical dataset for the Ottenby-2 core.

Depth (m)	TOC (wt%)	TS (wt%)	Hg (ppb)	Mo (ppm)	Hg/TOC (ppb/wt%)	Hg/S (ppb/wt%)	Δ ¹⁹⁹ Hg (‰)	Δ ²⁰⁰ Hg (‰)	Δ ²⁰¹ Hg (‰)
12.3	10.3	3.4	90	112	8.78	26.72			
12.4	12.6	3.5	199	185	15.86	56.20	0.002	-0.013	-0.008
12.8	6.9	9.2	202	108	29.55	21.97			
13.2	9.4	5.4	301	147	31.92	55.50			
13.8	8.6	4.4	314	186	36.48	71.34	-0.002	0.017	-0.051
14.3	2.0	0.5	46	30	23.09	20.00			
15.3	13.0	13.1	114	138	8.74	8.71			
16.0	12.1	9.0	185	274	15.26	20.53	-0.001	-0.019	0.015
16.2	10.9	14.5	934	226	85.42	64.26	0.007	0.041	0.010
16.7	9.8	13.1	789	230	80.35	60.28	0.029	0.008	0.018
17.2	4.4	7.1	233	84	53.46	32.91			
17.5	8.1	10.3	495	205	61.54	48.19	0.056	0.022	0.073
17.8	1.5	0.7	38	15	25.11	57.21			
18.1	12.6	10.5	103	184	8.21	9.83	0.055	0.009	0.061
18.3	13.0	11.1	134	124	10.30	12.11			
18.5	11.5	12.5	118	117	10.33	9.49			
18.9	11.5	14.4	316	75	27.42	22.00			
19.2	9.3	10.4	292	95	31.26	28.07			
19.4	5.7	2.2	98	19	17.15	44.60			
19.7	8.6	12.7	111	74	12.84	8.75			
20.2	12.1	10.6	289	58	23.85	27.26			
20.7	9.9	13.0	322	147	32.50	24.76			
21.2	9.4	10.6	126	198	13.40	11.91			
21.8	10.7	12.9	112	194	10.50	8.64			
22.3	9.9	14.2	164	152	16.49	11.56			
22.5	8.0	16.7	139	139	17.23	8.32			
23.1	9.1	15.8	150	146	16.45	9.50			
23.6	9.5	15.4	158	184	16.59	10.27			

solution was diluted with Milli-Q water to a final acid concentration of around 20% and stored at 4 °C for subsequent Hg isotope measurements. Instrumental mass bias was calibrated by an internal NIST 997 Tl standard solution supplied through Aridus II desolvation nebulizer system and the National Institute of Standards and Technology Standard Reference Material (NIST SRM) 3177 Hg standard sample. Mercury isotope compositions are expressed through nomenclature proposed by Bergquist and Blum (2007). Isotopic compositions are reported using delta notation (8) relative to the NIST SRM 3177 standard based on the equation:

$$\delta^{x}Hg(\text{\%o}) = \left. \left\{ \left[\left(^{x}Hg \middle/^{198}Hg\right)_{\textit{sample}} \middle/ \left(^{x}Hg \middle/^{198}Hg\right)_{\textit{standard}} \right] - 1 \right. \right\} \times 1000$$

where x is the mass number of each Hg isotope from 199 to 201. Mass independent fractionation is expressed by \triangle^x Hg that is defined though the following equation:

$$\Delta^x Hg = \delta^x Hg - (\delta^x Hg \times \beta)$$

in which x is the mass number of each Hg isotope (199, 200, and 201). β is a constant value based on kinetic MDF law (0.2520 for Δ^{199} Hg, 0.5024 for Δ^{200} Hg, and 0.7520 for Δ^{201} Hg). Analytical uncertainty of Hg isotopic compositions was evaluated by repeated analysis of the isotopic compositions of NIST SRM 3177. The average values of NIST SRM 3177 (0.01 \pm 0.06% for Δ^{199} Hg, 0.03 \pm 0.07% for Δ^{200} Hg, and - 0.01 \pm 0.05% for Δ^{201} Hg (± 2 s.d.)) are in good agreement with previous results (Bergquist and Blum, 2007; Zhou et al., 2021). Hg isotopes were only measured for zones III and VI (Fig. 2 and Table 1).

4. Results

The organic carbon isotope ($\delta^{13}C_{org}$, Fig. 2A) values remain relatively constant at -30.8% in the Miaolingian. During the Furongian, the $\delta^{13}C_{org}$ values increase to -28.4% at 18.1 m in the early Furongian *Olenus* Superzone, corresponding to the SPICE event (Saltzman et al., 2000; Gill et al., 2011; Zhao et al., 2022). In the mid-late Furongian, the $\delta^{13}C_{org}$ values remain constant at approximate -30.5% within the

Parabolina Superzone and subsequently rise to -28.0%, followed by a relatively gradual decrease within the *Peltura* Superzone. After that, the $\delta^{13}C_{org}$ values stay stable until end of the Furongian Series.

In the Miaolingian, TOC contents vary from 8.0 to 12.1 wt% with an average value of 9.8 wt% (n=9). During the Furongian, TOC contents are around 6.0 wt%, before exhibiting a continuously upward increase to around 13.0 wt% at \sim 18.1 m. After that, TOC contents diminish to 1.5 wt% at 17.8 m, followed by a gradual rise to 13.0 wt% at 15.3 m. Within Hg loading event IV, TOC contents are around 8.0 wt% (Fig. 2B).

During the Miaolingian, TS contents fluctuate between 10.6 and 16.7 wt% with an average value of 13.5 wt% (n = 9). In the Furongian, TS contents increase rapidly from 2.2 to 14.4 wt% and then remain at above 10.0 wt%. After that, TS contents display a gradual increase from 0.7 to \sim 13.5 wt% at \sim 15.0 m. Within Hg event IV, TS contents increase gradually from \sim 0.5 to \sim 9.0 wt% and then remain \sim 3.5 wt% (Fig. 2C).

Profiles of total Hg and Hg/TOC show an increase just before the SPICE event at around 20.0 to 21.0 m in the late Miaolingian (zone I of Fig. 2). In the Furongian, three elevated Hg anomalies are identified (Fig. 2): (i) the first Hg anomaly occurs during the SPICE event (zone II) at 18.0–20.0 m; (ii) the second anomaly, which shows the highest level of Hg (zone III), occurs after the SPICE event at 16.0–17.5 m; and (iii) the third Hg anomaly is observed in the late Furongian (zone IV) located at 12.5–14.5 m. In addition, the observed Hg anomalies vary from 202 to 934 ppb (median value: 314 ppb) and the background Hg contents are between 39 and 199 ppb with a median value of 118 ppb. Those values are above tenfold higher than the previously reported late Cambrian Hg enrichments (Pruss et al., 2019) and higher than the documented median Hg concentration (62.4 ppb) for key mass extinction and oceanic anoxic events through Earth's history (Grasby et al., 2019).

During loading event I, Hg/TS ratios are almost doubled before returning to background values ($\sim \! 10$ ppb/wt%). In the Furongian, Hg/TS ratios are around 25 ppb/wt% during loading event II. During event III, Hg/TS ratios vary between 33 and 65 ppb/wt% and subsequently decrease to background values. During loading event IV, the highest Hg/TS ratio reaches $\sim \! 71$ ppb/wt%, followed by a decrease towards $\sim \! 22$ ppb/wt%.

When Hg concentrations and Hg/TOC ratios display their highest

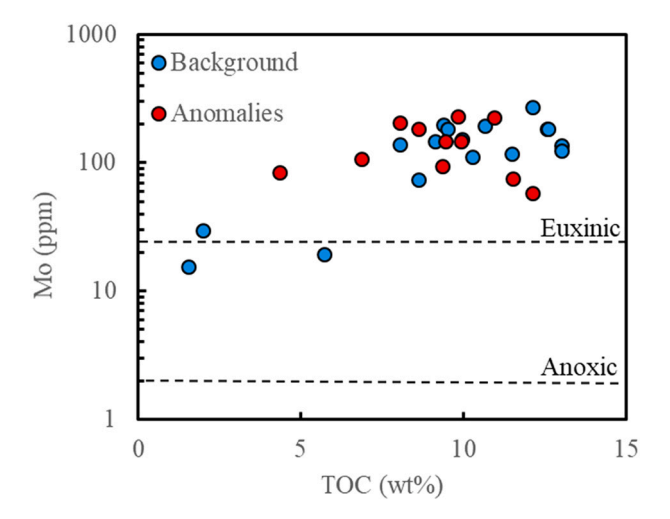


Fig. 3. Molybdenum (Mo) versus total organic carbon (TOC). The samples selected refer to Fig. 2D.

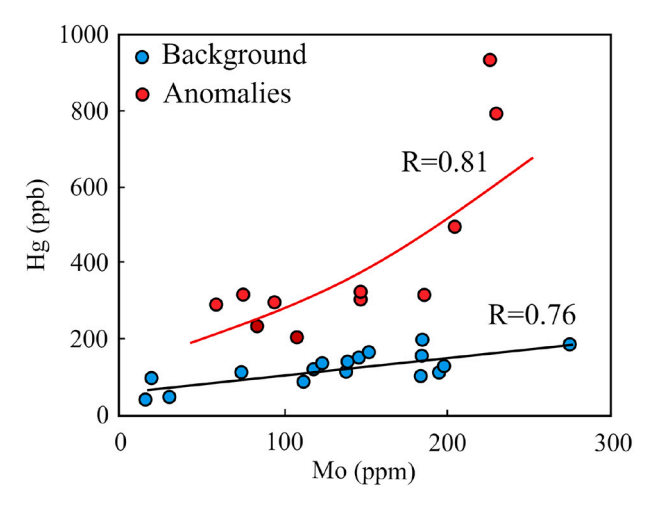


Fig. 4. Mercury (Hg) versus molybdenum (Mo). The samples selected refer to Fig. 2D. The significant level is above 99%.

concentrations in zone III, the even Hg-MIF values (Δ^{200} Hg; Fig. 2H) remain close to 0% and the odd Hg-MIFs (Δ^{199} Hg and Δ^{201} Hg; Fig. 2G and I) show a consistent decrease towards ~0%, suggesting

volcanogenic sources (Shen et al., 2019a).

Molybdenum concentrations were used to identify redox condition. Fig. 3 displays Mo concentrations in most samples are above 25 ppm. The relationship between Mo and Hg is used to assess potential mechanisms for Hg enrichments. Fig. 4 shows that Hg and Mo concentrations are linearly correlated in samples at Hg background level (R = 0.76, p < 0.01). However, they have an exponential correlation in Hg anomalous samples (R = 0.81, p < 0.01).

The dominant host phases of Hg are examined by crossplots of Hg versus TS and Hg versus TOC (Fig. 5A and B; Shen et al., 2019b, 2020). Fig. 5A shows that Hg has a significant correlation with TS in samples at Hg background level (R=0.88, P<0.01), whereas there is no statistical relationship in Hg anomalous samples. Fig. 5B displays that Hg and TOC are correlated with an R of 0.67 (P<0.01) in samples at Hg background level and that they are insignificantly correlated in Hg anomalous samples.

5. Discussion

5.1. Potential controls on late Cambrian Hg enrichments

Four Hg maximums are reported for the Miaolingian–Furongian succession in Ottenby-2 core (Fig. 2). The four Hg anomalies are identified by contemporaneous increases of Hg concentrations as well as Hg/TOC and Hg/TS ratios (zones I to IV; Fig. 2). The most elevated Hg concentrations measured (zone III) occur just after the SPICE event. This anomaly is characterized by concurrent increases of Hg concentrations, Hg/TOC and Hg/TS ratios, near-zero even Hg-MIF (Δ^{200} Hg), and near-zero to weakly positive odd Hg-MIFs (Δ^{199} Hg and Δ^{201} Hg). The youngest Hg anomaly (zone IV) exhibits a similar variation as Hg loading event III.

Sulfides and organic matter are important sinks for sequestrating Hg under reducing conditions (Shen et al., 2019b, 2020). Fig. 5 shows that Hg concentrations are significantly correlated to TS contents and are weakly correlated to TOC contents in samples at Hg background level. This suggests that sulfides are the dominant host phases of Hg, followed by organic matter (maybe as sulfurized organic matter). Although there is no statistical correlation for Hg anomalous samples, we consider that sulfides and organic matter remain important host phases, because both samples with background Hg values and anomalous values were deposited under the same redox conditions (Fig. 3).

These Hg enrichments could have resulted from three potential mechanisms: (1) terrestrial erosion processes that would have transported significant rocks into seawater (Grasby et al., 2017; Meixnerová et al., 2021; Shen et al., 2022); (2) reducing conditions that would have

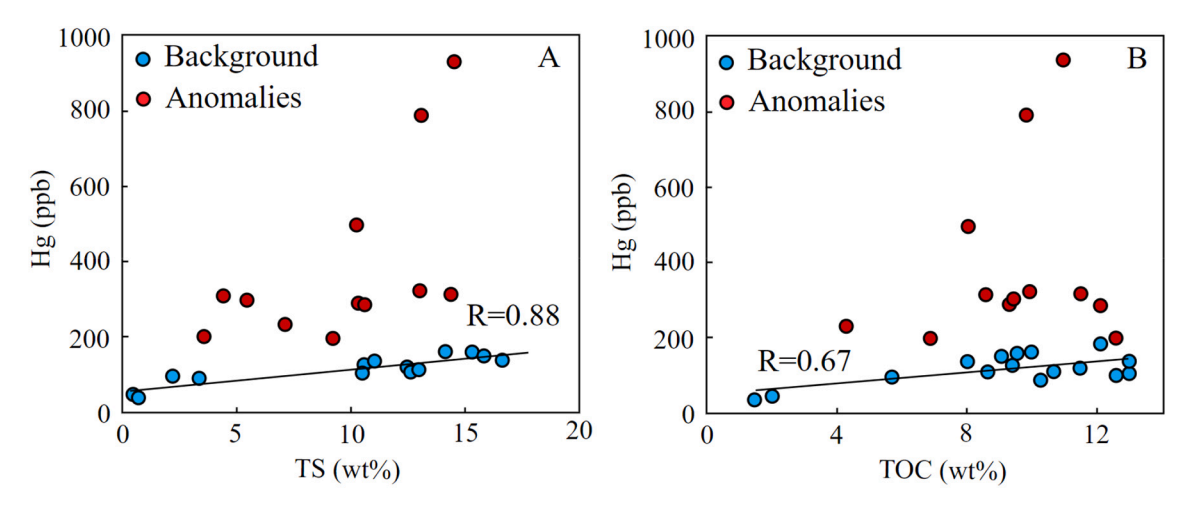


Fig. 5. A: Mercury (Hg) versus total sulfur (Mo), and (B) Mercury (Hg) versus total organic carbon (TOC). The samples selected refer to Fig. 2D. The significant level is above 99%.

L. Bian et al. Chemical Geology 599 (2022) 120846

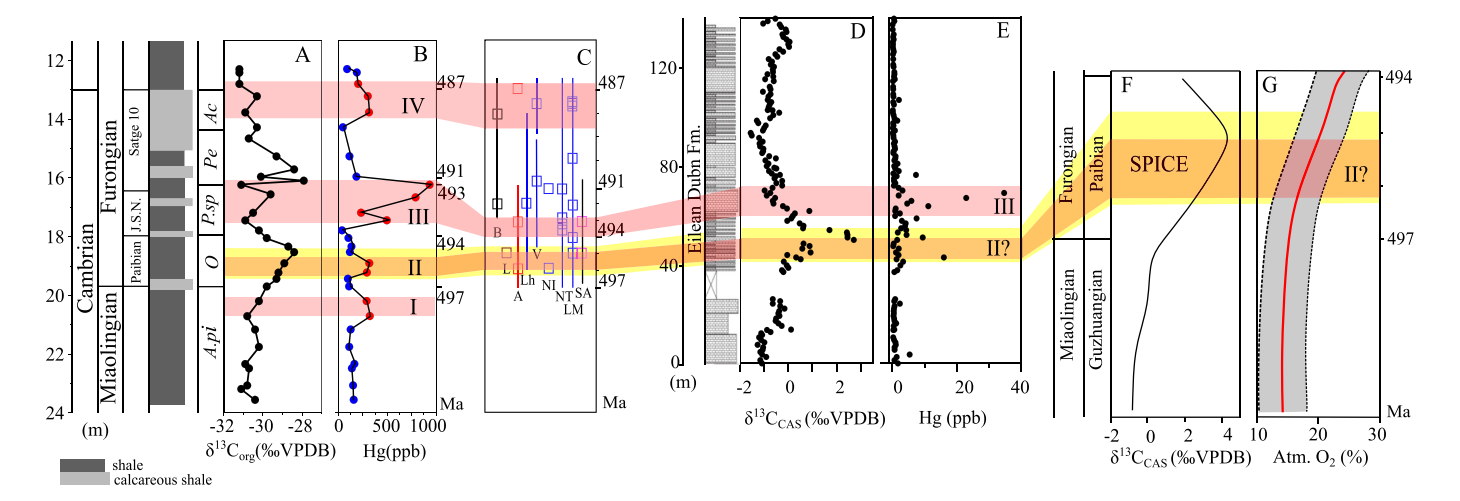


Fig. 6. Comparison of Hg anomalies in Baltica and Laurentia. Panels A and B are organic carbon isotope (δ¹³C_{org}) and Hg content in Baltica. The depositional age is identified by trilobites/graptolite biozones in Baltica (Peng et al., 2020; Zhao et al., 2022). Panel C: reported Furongian global volcanic events. B: Baltica, L: Laurentia, A: Avalonia, NG: Northern Gondwana, Lh: Lhasa Terrane, V: southern Variscan branch, NI: northern India, NT: northern Tianshan, LM: Liberian Massif, SA: southern Australian. Source data are provided in Table 2. Panels D and E: carbonate carbon isotope and Hg in Laurentia (Pruss et al., 2019). Panels F and G: carbonate carbon isotope and modeled late Cambrian atmospheric oxygen content (Saltzman et al., 2011).

promoted removal of continuous Hg supply from seawater (Grasby et al., 2019; Shen et al., 2019b, 2020); and (3) massive release of Hg from volcanic activity. Scenario (1) can be reasonably excluded, because previous studies reported an extremely low sedimentation rate in the Alum Shale (< 6 mm/ka; Sturesson et al., 2005; Sørensen et al., 2020). Terrestrial particles that may have contained Hg were not delivered fast enough into the Baltoscandian Basin to explain Hg anomalies. Scenario (2) may have been responsible for elevated Hg background values but cannot explain Hg anomalous horizons. At first, we used Mo concentrations to recognize redox conditions in Baltoscandian Basin (Scott and Lyons, 2012; Gill et al., 2021). Generally, 2 < Mo < 25 indicates anoxic conditions and Mo > 25 suggests euxinic conditions. Fig. 3 shows that all samples were deposited into anoxic to euxinic (reducing) conditions. In addition, the Hg/Mo ratio is commonly constant and strongly correlated (Shen et al., 2019b; Meixnerová et al., 2021). Therefore, the linear correlation between Mo and Hg concentrations in samples at Hg background level suggests that the relatively high Hg background values could be attributed to reducing conditions and continuous Hg supply from seawater (Fig. 4). Therefore, we argue that the most plausible scenario for explaining Hg anomalies is volcanic activity. This inference is also supported by elevated Hg concentrations, Hg/TOC and Hg/TS ratios, near-zero Hg MIFs in loading events III and IV, and gradually decreased odd Hg MIFs in loading event III (Fig. 2. Grasby et al., 2017; Shen et al., 2019a, 2020). These attributes also reinforce the fact that scenario (3) is a reasonable mechanism to explain Hg anomalies, i.e., late Cambrian Hg loading events were associated with volcanic activities.

5.2. Comparison with the Laurentian Hg enrichments

Previous studies examining Hg enrichments across the late Cambrian are scarce. Hitherto, only one study documented Hg enrichments in carbonate rocks of the late Cambrian Eilean Dubh Formation, northern Scotland, and attributed them to redox oscillations of ocean water based on increased glauconite contents and the absence of reported large igneous provinces (Pruss et al., 2019). Their dataset and our new one show that the climax of the SPICE event occurs prior to the highest Hg concentrations (Figs. 1 and 6). By combining an in-depth examination of biostratigraphic fossils with organic carbon isotopic signature (Fig. 1), we suggest that the highest Hg concentrations (zone III) are after the SPICE event rather than within the SPICE event. In addition, we consider that Hg anomalies in Laurentia (Scotland) and Baltica (this study) could

have been contemporaneous through the constraint of positive carbon isotope excursion during the SPICE event (Fig. 6).

Mercury concentrations range from 30 to 934 ppb in our samples but are below 40 ppb in Laurentia (Fig. 5B and E). We explore different mechanisms to explain this difference: (1) different Hg host phases. Most samples in Laurentia display low organic matter contents (<0.1 wt%) and detrital mineral contents (<10 wt%) that are likely responsible for fixing Hg, whereas the dominant Hg host phases in our samples are probably sulfides and organic matter (Fig. 5). Previous studies suggested that organic matter and sulfides have higher adsorption capabilities for Hg sequestration (Wolfenden et al., 2005; Skyllberg and Drott, 2010; Chakraborty et al., 2015; Shen et al., 2019a). We thus argue that the variations in content and type of host phases might partially explain different Hg concentrations in these two areas; (2) different redox conditions may affect the fixation rate of Hg. Sediments in Laurentia were deposited under oxic to dysoxic conditions, while our studied samples were deposited under extremely oxygen-depleted conditions (Fig. 3). The reducing conditions could promote Hg fixation by forming organic-Hg complexes and Hg-sulfides (Ravichandran, 2004; Duan et al., 2016; Shen et al., 2019a); and (3) other factors, such as seawater inflow and sedimentation rate (Shen et al., 2019a, 2022).

We can observe a weakly negative carbon isotope excursion after the most pronounced Hg anomaly in Laurentia (Figs. 6D-E). However, there is a positive organic carbon isotope excursion in the Peltura Superzone, likely following loading event III in the Parabolina spinulosa Superzone of Ottenby-2 core (Fig. 5A). We attribute this result to the absence of Leptoplastus and Protopeltura Superzones in the Ottenby-2 core during the mid-late Jiangshanian Stage. Zhao et al. (2022) investigated the late Cambrian organic carbon isotope in the Alum Shale and showed that there is a negative carbon isotope excursion within the Leptoplastus Superzone just after loading event III (Parabolina spinulosa Superzone). During loading events I and II, the $\delta^{13} C_{\text{org}}$ values show a continuous increase. The positive organic carbon isotope excursion commonly results from increased marine phytoplankton productivity and/or increased organic matter preservation under reducing conditions (Kump and Arthur, 1999). Previous studies proposed that oceanic anoxia was mainly responsible for organic carbon isotope excursion during the SPICE event (Gill et al., 2011; Dahl et al., 2014; Schiffbauer et al., 2017; LeRoy and Gill, 2019; Pruss et al., 2019). Therefore, we suggest that the negative organic carbon isotope excursion caused by volcanism may have been inhibited owing to massive organic carbon burial.

Although large igneous provinces have not been reported during the

Table 2 Summary of global volcanic activities between \sim 497 and \sim 487 Ma.

Location	Sampling	Ages	Dating	Magmatism type	References
	Outer margin of Baltica (Köli Nappe)	488 ± 5	U–Pb	subduction	Claesson et al., 1983; Barnes et al., 2019
Baltica	Outer margin of Baltica (Köli Nappe)	$\textbf{492} \pm \textbf{1}$	U–Pb Rb–Sr	subduction	Claesson et al., 1988; Barnes et al., 2019
Avalonia	/	$493 \pm 2,496 \pm 5$	U–Pb	subduction	Vozárová et al., 2010
Laurentia	Grampian-Taconic forearc	495 peak	U–Pb	subduction	O'Sullivan and Chew, 2020
	Lhasa Terrane	492 ± 4	U–Pb	subduction	Zhu et al., 2012
	North India	491, 496	U–Pb	subduction	Zhu et al., 2012
	North Tian Shan	$491 \pm 3, 492.6 \pm 1.6, 493.5 + \\ 3.7, 493 \pm 4$	U–Pb	subduction	Rojas-Agramonte et al., 2014; Alexeiev et al., 2019
	Southern Variscan branch (Sardinia, Italy)	491.7 ± 3.5	U–Pb	subduction	Oggiano et al., 2010
Northern Gondwana	Liberian Massif - Viana do Bolo	488 ± 4	U–Pb	subduction	Montero et al., 2009; García-Arias et al., 2018
	Liberian Massif - Sanabria	488 ± 6	U–Pb	subduction	Díez Montes, 2006; García-Arias et al., 2018
	Liberian Massif - Puebla de Sanabria	488 \pm 3, 490 \pm 2, 492 \pm 4	U–Pb	subduction	Montero et al., 2007
	Liberian Massif - Hiendelaencin	494 \pm 4, 495 \pm 5	U–Pb Rb–Sr	subduction	Montero et al., 2007
	Southern Australia, Western Victoria	492.8 \pm 1.3, 495 \pm 1.2	U–Pb	subduction	Foden et al., 2006, 2020
Southern Gondwana	Mount Read Volcanic Belt, Western Tasmania, Australia	$496 \pm 0.9, 497.3 \pm 0.9$	U–Pb	collision	Mortensen et al., 2015

late Cambrian, we examined the global late Cambrian magmatic activities and remarked intense global volcanic activities along the plate subduction zones (Fig. 1 and Table 2). Those volcanic activities probably resulted in the pronounced Hg anomalies observed in Baltica and Laurentia. There is not enough evidence to conclude whether Hg events I, II, and IV could be identified for other continents. However, we consider that they were likely a sequel of massive volcanic activities that occurred before, during, and after the SPICE event because of the consistent increase of simulated atmospheric oxygen from late Miaolingian to early Furongian (Fig. 6; Saltzman et al., 2011).

5.3. Intensive volcanic activity as potential trigger for major environmental perturbation

The late Cambrian interval was a period that witnessed recurrent mass extinction events (Bambach et al., 2004; Pruss et al., 2010; Saltzman et al., 2015). Previous studies proposed that widespread oceanic anoxia was mostly responsible for mass extinction during the SPICE event in early Furongian (Saltzman et al., 2000; Dahl et al., 2014; LeRoy and Gill, 2019; Gill et al., 2011, 2021). Dahl et al. (2014) proposed two stages for the SPICE event: the first stage had a widespread oceanic euxinia that was associated with a well-known trilobite extinction event, and the second stage had less euxinic conditions and enhanced nutrient availability that would have fueled phytoplankton diversification. However, the SPICE event was followed by the mid-late Furongian mass extinction events (Saltzman et al., 2015; Kröger et al., 2019; Zhang et al., 2021).

Although volcanic activity was unlikely responsible for the SPICE event, it could have favored mass extinction by stressing the marine ecosystem (Bauer et al., 2021; Schoepfer et al., 2022). Massive volcanic activity could release light carbon isotopes to the surface of Earth and contribute to elevated organic matter burial, which is responsible for the widely recognized negative carbon isotope excursion following Hg anomaly (Kump and Arthur, 1999; Sanei et al., 2012; Lindström et al., 2019; Shen et al., 2019a, 2022). The most pronounced Hg anomaly in Baltica and Laurentia was followed by a negative carbon isotope excursion, likely suggesting the observed Hg enrichments were not a localized phenomenon and may have been associated with high extinction rates in the mid-late Furongian (Bambach et al., 2004; Pruss et al., 2010; Saltzman et al., 2015; Zhang et al., 2021). In addition, the recognized volcanic activity (loading events I to IV) may have been partially responsible for elevated atmospheric oxygen in the late Cambrian (Saltzman et al., 2011). We acknowledge that our new dataset

is limited to a single location, preventing us from making a robust case for a potential global influence. However, we cautiously speculate that massive volcanic activity could have released significant amounts of greenhouse gases (¹³C-depleted CO₂ and ³⁴S-depleted SO₂), progressively leading to major environmental perturbations. Ultimately, these important changes pushed the ecosystem towards a tipping point that may have in some measure contributed to the recurrent mass extinction events that occurred during the late Cambrian (Gaillard and Scaillet, 2014; Saltzman et al., 2015; Fan et al., 2020; Cui et al., 2021). Additional work is required to confirm or reject that hypothesis.

6. Conclusion

The late Cambrian mercury (Hg) records obtained from the Alum Shale core in southern Sweden show four distinct Hg anomalies. Despite the occurrence of reducing conditions and continuous Hg supply from seawater that could favor significant concentrations of Hg fixation (background level), we argue that the four Hg anomalies resulted from volcanic activities. This is characterized by the high values in total Hg as well as Hg/TOC and Hg/TS ratios for Hg loading events I to IV, and nearzero even Hg mass independent fractionation (even MIF; $\Delta^{200}\text{Hg})$ and near-zero to weakly positive odd Hg MIFs (Δ^{199} Hg and Δ^{201} Hg) for Hg loading events III-IV. The most profound Hg anomalies observed in Baltica were synchronous with Hg anomalies recorded in Laurentian sedimentary archives, suggesting that these Hg anomalies may have also been recorded in other continents. Furthermore, all these Hg anomalies were intimately associated with the late Cambrian biological extinction, underscoring the needs to examine in future studies the late Cambrian volcanic effects at a global scale.

Declaration of Competing Interest

No.

Acknowledgements

All authors thank Editor-in-Chief Dr. Michael E. Böttcher for handling this manuscript and thank Dr. Jun Shen and two other anonymous reviewers for constructive comments. We thank Dr. L.M.E. Pervical for scientific advices. We acknowledge support from the GeoCenter Denmark project 2017-3 (awarded to NS and AN), NSF-EAR grant 2051199 (AC), CSC scholarship and the Spackman award (BL), and Grant No. SKLOG202115.

References

- Alexeiev, D.V., Kröner, A., Kovach, V.P., Tretyakov, A.A., Rojas-Agramonte, Y., Degtyarev, K.E., Mikolaichuk, A.V., Wong, J., Kiselev, V.V., 2019. Evolution of Cambrian and early Ordovician arcs in the Kyrgyz North Tianshan: Insights from U-Pb zircon ages and geochemical data. Gondwana Res. 66, 93–115. https://doi.org/ 10.1016/j.gr.2018.09.005.
- Bambach, R.K., Knoll, A.H., Wang, S.C., 2004. Origination, extinction, and mass depletions of marine diversity. Paleobiology 30 (4), 522–542. https://doi.org/ 10.1666/0094-8373(2004)030 <0522: OEAMDO > 2.0.CO;2.
- Barnes, C., Majka, J., Schneider, D., Walczak, K., Bukała, M., Kośmińska, K., Tokarski, T., Karlsson, A., 2019. High-spatial resolution dating of monazite and zircon reveals the timing of subduction-exhumation of the Vaimok Lens in the Seve Nappe complex (Scandinavian Caledonides). Contribut. Mineral. Petrol. 174, 1–18. https://doi.org/ 10.1007/s00410-018-1539-1.
- Bauer, K.W., Bottini, C., Frei, R., Asael, D., Planavsky, N.J., Francois, R., McKenzie, N.R., Erba, E., Crowe, S.A., 2021. Pulsed volcanism and rapid oceanic deoxygenation during Oceanic Anoxic Event 1a. Geology 49 (12), 1452–1456. https://doi.org/10.1130/G49065.1.
- Bergquist, B.A., Blum, J.D., 2007. Mass-dependent and-independent fractionation of Hg isotopes by photoreduction in aquatic systems. Science 318, 417–420. https://doi. org/10.1126/science.1148050.
- Bian, L., Schovsbo, N.H., Chappaz, A., Zheng, X., Nielsen, A.T., Ulrich, T., Wang, X., Dai, S., Galloway, J.M., Małachowska, A., Xu, X., Sanei, H., 2021. Molybdenumuranium-vanadium geochemistry in the lower Paleozoic Alum Shale of Scandinavia: Implications for vanadium exploration. Int.J. Coal Geol. 239, 103730 https://doi.org/10.1016/j.coal.2021.103730.
- Blum, J.D., Sherman, L.S., Johnson, M.W., 2014. Mercury isotopes in earth and environmental sciences. Annu. Rev. Earth Planet. Sci. 42, 249–269. https://doi.org/ 10.1146/annurey-earth-050212-124107.
- Chakraborty, P., Sarkar, A., Vudamala, K., Naik, R., Nath, B.N., 2015. Organic matter—a key factor in controlling mercury distribution in estuarine sediment. Mar. Chem. 173, 302–309. https://doi.org/10.1016/j.marchem.2014.10.005.
- Chen, J., Hintelmann, H., Feng, X., Dimock, B., 2012. Unusual fractionation of both odd and even mercury isotopes in precipitation from Peterborough, ON, Canada: Conclude Company Acts 09, 32 46. https://doi.org/10.1016/j.jcps.2012.05.005
- Geochim. Cosmochim. Acta 90, 33–46. https://doi.org/10.1016/j.gca.2012.05.005. Claesson, S., Klingspor, I., Stephens, M.B., 1983. U-Pb and Rb-Sr isotopic data on an Ordovician volcanic-subvolcanic complex from the Tjopasi Group, Köli Nappes, Swedish Caledonides. Geol. Fören. Stockh. Förh. 105, 9–15. https://doi.org/
- Claesson, S., Stephens, M.B., Klingspor, I., 1988. U-Pb zircon dating of felsic intrusions. Middle Köli Nappes, central Scandinavian Caledonides. Norw. J. Geol. 68, 89–97. http://www.geologi.no/images/NJG_articles/NGT_68_2_089–097.pdf.
- Cui, Y., Li, M., Van Soelen, E.E., Peterse, F., Kürschner, W.M., 2021. Massive and rapid predominantly volcanic CO2 emission during the end-Permian mass extinction. Proc. Natl. Acad. Sci. U. S. A. 118, e2014701118 https://doi.org/10.1073/pnas. 2014701118.
- Dahl, T.W., Boyle, R.A., Canfield, D.E., Connelly, J.N., Gill, B.C., Lenton, T.M., Bizzarro, M., 2014. Uranium isotopes distinguish two geochemically distinct stages during the later Cambrian SPICE event. Earth Planet. Sci. Lett. 401, 313–326. https://doi.org/10.1016/j.epsl. 2014.05.043.
- Díez Montes, A., 2006. La Geología del Dominio Ollo de Sapo en las comarcas de Sanabria y Terra do Bolo. PhD Thesis. Universidad de Salamanca, p. 496. http://info. igme.es/SidPDF/079000/728/79728_0000029.pdf.
- Duan, Y., Han, D.S., Batchelor, B., Abdel-Wahab, A., 2016. Synthesis, characterization, and application of pyrite for removal of mercury. Colloids Surf. A Physicochem. Eng. Asp. 490, 326–335. https://doi.org/10.1016/j.colsurfa.2015.11.057.
- Edwards, B.A., Kushner, D.S., Outridge, P.M., Wang, F., 2021. Fifty years of volcanic mercury emission research: Knowledge gaps and future directions. Sci. Total Environ. 757, 143800 https://doi.org/10.1016/j.scitotenv.2020.143800.
- Elrick, M., Rieboldt, S., Saltzman, M., McKay, R.M., 2011. Oxygen-isotope trends and seawater temperature changes across the late Cambrian Steptoean positive carbonisotope excursion (SPICE event). Geology 39, 987–990. https://doi.org/10.1130/ G32109.1.
- Fan, J.X., Shen, S.Z., Erwin, D.H., Sadler, P.M., MacLeod, N., Cheng, Q.M., Hou, X.D., Yang, J., Wang, X.D., Wang, Y., Zhang, H., 2020. A high-resolution summary of Cambrian to early Triassic marine invertebrate biodiversity. Science 367, 272–277. https://doi.org/10.1126/science.aax4953.
- Fitzgerald, W.F., Lamborg, C.H., Hammerschmidt, C.R., 2007. Marine biogeochemical cycling of mercury. Chem. Rev. 107, 641–662. https://doi.org/10.1021/cr050353m.
- Foden, J., Elburg, M.A., Dougherty-Page, J., Burtt, A., 2006. The timing and duration of the Delamerian Orogeny: correlation with the Ross Orogen and implications for Gondwana assembly. J. Geol. 114, 189–210. https://doi.org/10.1086/499570.
- Foden, J., Elburg, M., Turner, S., Clark, C., Blades, M.L., Cox, G., Collins, A.S., Wolff, K., George, C., 2020. Cambro-Ordovician magmatism in the Delamerian orogeny: Implications for tectonic development of the southern Gondwanan margin. Gondwana Res. 81, 490–521. https://doi.org/10.1016/j.gr.2019.12.006.
- Gaillard, F., Scaillet, B., 2014. A theoretical framework for volcanic degassing chemistry in a comparative planetology perspective and implications for planetary atmospheres. Earth Planet. Sci. Lett. 403, 307–316. https://doi.org/10.1016/j. epsl.2014.07.009.
- García-Arias, M., Díez-Montes, A., Villaseca, C., Blanco-Quintero, I.F., 2018. The Cambro-Ordovician Ollo de Sapo magmatism in the Iberian Massif and its Variscan evolution: a review. Earth Sci. Rev. 176, 345–372. https://doi.org/10.1016/j. earscirev.2017.11.004.

- Gill, B.C., Lyons, T.W., Young, S.A., Kump, L.R., Knoll, A.H., Saltzman, M.R., 2011. Geochemical evidence for widespread euxinia in the later Cambrian Ocean. Nature 469, 80–83. https://doi.org/10.1038/nature09700.
- Gill, B.C., Dahl, T.W., Hammarlund, E.U., LeRoy, M.A., Gordon, G.W., Canfield, D.E., Anbar, A.D., Lyons, T.W., 2021. Redox dynamics of later Cambrian oceans. Palaeogeogra. Palaeoclimatol. Palaeoecol. 581, 110623 https://doi.org/10.1016/j.palaeo.2021.110623.
- Grasby, S.E., Shen, W., Yin, R., Gleason, J.D., Blum, J.D., Lepak, R.F., Hurley, J.P., Beauchamp, B., 2017. Isotopic signatures of mercury contamination in latest Permian oceans. Geology 45 (1), 55–58. https://doi.org/10.1130/G38487.1.
- Grasby, S.E., Them II, T.R., Chen, Z., Yin, R., Ardakani, O.H., 2019. Mercury as a proxy for volcanic emissions in the geologic record. Earth Sci. Rev. 196, 102880 https:// doi.org/10.1016/j.earscirev.2019.102880.
- Janssen, S.E., Schaefer, J.K., Barkay, T., Reinfelder, J.R., 2016. Fractionation of mercury stable isotopes during microbial methylmercury production by iron-and sulfatereducing bacteria. Environ. Sci. Technol. 50, 8077–8083. https://doi.org/10.1021/ acs.est.6b00854.
- Jiao, W.J., Li, Y.X., Yang, Z.Y., 2018. Paleomagnetism of a well-dated marine succession in South China: a possible late Cambrian true polar wander (TPW). Phys. Earth Planet. Int. 277, 38–54. https://doi.org/10.1016/j.pepi.2018.01.009.
- Jones, D.S., Martini, A.M., Fike, D.A., Kaiho, K., 2017. A volcanic trigger for the late Ordovician mass extinction? Mercury data from South China and Laurentia. Geology 45, 631–634. https://doi.org/10.1130/G38940.1.
- Kröger, B., Franeck, F., Rasmussen, C.M., 2019. The evolutionary dynamics of the early Palaeozoic marine biodiversity accumulation. Proc. Royal Soc. B 286 (1909), 20191634. https://doi.org/10.1098/rspb.2019.1634.
- Kump, L.R., Arthur, M.A., 1999. Interpreting carbon-isotope excursions: carbonates and organic matter. Chem. Geol. 161 (1–3), 181–198. https://doi.org/10.1016/S0009-2541(99)00086-8
- Lepak, R.F., Janssen, S.E., Engstrom, D.R., Krabbenhoft, D.P., Tate, M.T., Yin, R., Fitzgerald, W.F., Nagorski, S.A., Hurley, J.P., 2020. Resolving Atmospheric Mercury Loading and Source Trends from Isotopic Records of Remote North American Lake Sediments. Environ. Sci. Technol. 54, 9325–9333. https://doi.org/10.1021/acs. est.0c00579.
- LeRoy, M.A., Gill, B.C., 2019. Evidence for the development of local anoxia during the Cambrian SPICE event in eastern North America. Geobiology 17 (4), 381–400. https://doi.org/10.1111/gbi.12334.
- Lindström, S., Sanei, H., Van De Schootbrugge, B., Pedersen, G.K., Lesher, C.E., Tegner, C., Heunisch, C., Dybkjær, K., Outridge, P.M., 2019. Volcanic mercury and mutagenesis in land plants during the end-Triassic mass extinction. Sci. Adv. 5 (10), eaaw4018. https://doi.org/10.1126/sciadv.aaw4018.
- Mason, R.P., Sheu, G.R., 2002. Role of the ocean in the global mercury cycle. Glob. Biogeochem. Cycles 16 (4). https://doi.org/10.1029/2001GB001440.
- Mead, C., Lyons, J.R., Johnson, T.M., Anbar, A.D., 2013. Unique Hg stable isotope signatures of compact fluorescent lamp-sourced Hg. Environ. Sci. Technol. 47, 2542–2547. https://doi.org/10.1021/es303940p.
- Meixnerová, J., Blum, J.D., Johnson, M.W., Stüeken, E.E., Kipp, M.A., Anbar, A.D., Buick, R., 2021. Mercury abundance and isotopic composition indicate subaerial volcanism prior to the end-Archean "whiff" of oxygen. Proc. Natl. Acad. Sci. U. S. A. 118, e2107511118 https://doi.org/10.1073/pnas.2107511118.
- Montero, P., Bea, F., González-Lodeiro, F., Talavera, C., Whitehouse, M.J., 2007. Zircon ages of the metavolcanic rocks and metagranites of the Ollo de Sapo Domain in Central Spain: implications for the Neoproterozoic to early Palaeozoic evolution of Iberia. Geol. Mag. 144, 963–976. https://doi.org/10.1017/S0016756807003858.
- Montero, P., Talavera, C., Bea, F., Lodeiro, F.G., Whitehouse, M.J., 2009. Zircon geochronology of the Ollo de Sapo Formation and the age of the Cambro-Ordovician rifting in Iberia. J. Geol. 117, 174–191. https://doi.org/10.1086/595017.
- Mortensen, J.K., Gemmell, J.B., McNeill, A.W., Friedman, R.M., 2015. High-precision U-Pb zircon chronostratigraphy of the Mount Read Volcanic belt in Western Tasmania, Australia: Implications for VHMS deposit formation. Econ. Geol. 110, 445–468. https://doi.org/10.2113/econgeo.110.2.445.
- Nielsen, A.T., Ahlberg, P., 2019. The Miaolingian, a new name for the 'Middle' Cambrian (Cambrian Series 3): identification of lower and upper boundaries in Baltoscandia. Gff 141 (2), 162–173. https://doi.org/10.1080/11035897.2019.1621374.
- Nielsen, A.T., Schovsbo, N.H., 2006. Cambrian to basal Ordovician lithostratigraphy in southern Scandinavia. Bull. Geol. Soc. Denmark 53, 47–92.
- Nielsen, A.T., Schovsbo, N.H., 2015. The regressive Early-Mid Cambrian 'Hawke Bay Event'in Baltoscandia: epeirogenic uplift in concert with eustasy. Earth Sci. Rev. 151, 288–350. https://doi.org/10.1016/j.earscirev.2015.09.012.
- Obrist, D., Agnan, Y., Jiskra, M., Olson, C.L., Colegrove, D.P., Hueber, J., Moore, C.W., Sonke, J.E., Helmig, D., 2017. Tundra uptake of atmospheric elemental mercury drives Arctic mercury pollution. Nature 547, 201–204. https://doi.org/10.1038/ 2007.
- Oggiano, G., Gaggero, L., Funedda, A., Buzzi, L., Tiepolo, M., 2010. Multiple early Paleozoic volcanic events at the northern Gondwana margin: U–Pb age evidence from the Southern Variscan branch (Sardinia, Italy). Gondwana Res. 17, 44–58. https://doi.org/10.1016/j.gr.2009.06.001.
- O'Sullivan, G.J., Chew, D.M., 2020. The clastic record of a Wilson Cycle: evidence from detrital apatite petrochronology of the Grampian-Taconic fore-arc. Earth Planet. Sci. Lett. 552, 116588 https://doi.org/10.1016/j.epsl.2020.116588.
- Outridge, P.M., Mason, R.P., Wang, F., Guerrero, S., Heimburger-Boavida, L.E., 2018. Updated global and oceanic mercury budgets for the United Nations Global Mercury Assessment 2018. Environ. Sci. Technol. 52, 11466–11477. https://doi.org/ 10.1021/acs.est.8b01246.

- Peng, S.C., Babcock, L.E., Ahlberg, P., 2020. The Cambrian Period. In: Geologic time scale 2020. Elsevier, pp. 565–629. https://doi.org/10.1016/B978-0-12-824360-2.00010-X
- Percival, L.M., Bergquist, B.A., Mather, T.A., Sanei, H., 2021. Sedimentary Mercury Enrichments as a Tracer of Large Igneous Province Volcanism. Large Igneous Provinces: A Driver of Global Environmental and Biotic Changes, pp. 247–262. https://doi.org/10.1002/9781119507444.ch11.
- Petersen, H.I., Schovsbo, N.H., Nielsen, A.T., 2013. Reflectance measurements of zooclasts and solid bitumen in lower Paleozoic shales, southern Scandinavia: Correlation to vitrinite reflectance. Int. J. Coal Geol. 114, 1–18. https://doi.org/ 10.1016/j.coal. 2013.03.013.
- Pruss, S.B., Finnegan, S., Fischer, W.W., Knoll, A.H., 2010. Carbonates in skeleton-poor seas: new insights from Cambrian and Ordovician strata of Laurentia. Palaios 25 (2), 73–84. https://doi.org/10.2110/palo.2009.p09-101r.
- Pruss, S.B., Jones, D.S., Fike, D.A., Tosca, N.J., Wignall, P.B., 2019. Marine anoxia and sedimentary mercury enrichments during the late Cambrian SPICE event in northern Scotland. Geology 47, 475–478. https://doi.org/10.1130/G45871.1.
- Pyle, D.M., Mather, T.A., 2003. The importance of volcanic emissions for the global atmospheric mercury cycle. Atmospheric Environ. 37 (36), 5115–5124. https://doi. org/10.1016/j.atmosenv. 2003.07.011.
- Racki, G., Rakociński, M., Marynowski, L., Wignall, P.B., 2018. Mercury enrichments and the Frasnian-Famennian biotic crisis: a volcanic trigger proved. Geology 46, 543–546. https://doi.org/10.1130/G40233.1.
- Ravichandran, M., 2004. Interactions between mercury and dissolved organic matter—a review. Chemosphere 55 (3), 319–331. https://doi.org/10.1016/j.chemosphere.2003.11.011.
- Rojas-Agramonte, Y., Kröner, A., Alexeiev, D.V., Jeffreys, T., Khudoley, A.K., Wong, J., Geng, H., Shu, L., Semiletkin, S.A., Mikolaichuk, A.V., Kiselev, V.V., 2014. Detrital and igneous zircon ages for supracrustal rocks of the Kyrgyz Tianshan and palaeogeographic implications. Gondwana Res. 26, 957–974. https://doi.org/10.1016/j.gr.2013.09.005
- Saltzman, M.R., Ripperdan, R.L., Brasier, M.D., Lohmann, K.C., Robison, R.A., Chang, W. T., Peng, S., Ergaliev, E.K., Runnegar, B., 2000. A global carbon isotope excursion (SPICE) during the late Cambrian: relation to trilobite extinctions, organic-matter burial and sea level. Palaeogeogr. Palaeoclimatol. Palaeoecol. 162, 211–223. https://doi.org/10.1016/S0031-0182(00)00128-0.
- Saltzman, M.R., Young, S.A., Kump, L.R., Gill, B.C., Lyons, T.W., Runnegar, B., 2011.
 Pulse of atmospheric oxygen during the late Cambrian. Proc. Natl. Acad. Sci. U. S. A.
 108 (10), 3876–3881. https://doi.org/10.1073/pnas.1011836108.
- Saltzman, M.R., Edwards, C.T., Adrain, J.M., Westrop, S.R., 2015. Persistent oceanic anoxia and elevated extinction rates separate the Cambrian and Ordovician radiations. Geology 43, 807–810. https://doi.org/10.1130/G36814.1.
- Sanei, H., Grasby, S.E., Beauchamp, B., 2012. Latest Permian mercury anomalies. Geology 40, 63–66. https://doi.org/10.1130/G32596.1
- Sanei, H., Petersen, H.I., Schovsbo, N.H., Jiang, C., Goodsite, M.E., 2014. Petrographic and geochemical composition of kerogen in the Furongian (U. Cambrian) Alum Shale, Central Sweden: Reflections on the petroleum generation potential. Int. J. Coal Geol. 132, 158–169. https://doi.org/10.1016/j.coal.2014.08.010.
- Schiffbauer, J.D., Huntley, J.W., Fike, D.A., Jeffrey, M.J., Gregg, J.M., Shelton, K.L., 2017. Decoupling biogeochemical records, extinction, and environmental change during the Cambrian SPICE event. Sci. Adv. 3, e1602158 https://doi.org/10.1126/ sciadv.1602158.
- Schoepfer, S.D., Shen, J., Sano, H., Algeo, T.J., 2022. Onset of environmental disturbances in the Panthalassic Ocean over one million years prior to the Triassic-Jurassic boundary mass extinction. Earth Sci. Rev. 224, 103870 https://doi.org/ 10.1016/j.earscirev.2021.103870.
- Schovsbo, N.H., 2001. Why barren intervals? A taphonomic case study of the Scandinavian Alum Shale and its faunas. Lethaia 34 (4), 271–285. https://doi.org/ 10.1111/j.1502-3931.2001. tb00056.x.
- Scotese, C.R., 2001. Paleomap Project. Available online at. www.scotese.com.
 Scott, C., Lyons, T.W., 2012. Contrasting molybdenum cycling and isotopic properties in euxinic versus non-euxinic sediments and sedimentary rocks: refining the paleoproxies. Chem. Geol. 324, 19–27. https://doi.org/10.1016/j.chem.eo.2012.05.012
- Selin, N.E., 2009. Global biogeochemical cycling of mercury: a review. Annu. Rev. Environ. Resour. 34, 43–63. https://doi.org/10.1146/annurev. environ 051308 084314
- Shen, J., Chen, J., Algeo, T.J., Yuan, S., Feng, Q., Yu, J., Zhou, L., O'Connell, B., Planavsky, N.J., 2019a. Evidence for a prolonged Permian–Triassic extinction interval from global marine mercury records. Nat. Commun. 10, 1–9. https://doi. org/10.1038/s41467-019-09620-0.

- Shen, J., Algeo, T.J., Chen, J., Planavsky, N.J., Feng, Q., Yu, J., Liu, J., 2019b. Mercury in marine Ordovician/Silurian boundary sections of South China is sulfide-hosted and non-volcanic in origin. Earth Planet. Sci. Lett. 511, 130–140. https://doi.org/ 10.1016/i.epsl.2019.01.028.
- Shen, J., Feng, Q., Algeo, T.J., Liu, J., Zhou, C., Wei, W., Liu, J., Them II, T.R., Gill, B.C., Chen, J., 2020. Sedimentary host phases of mercury (Hg) and implications for use of Hg as a volcanic proxy. Earth Planet. Sci. Lett. 543, 116333 https://doi.org/10.1016/j.epsl.2020.116333.
- Shen, J., Yin, R., Zhang, S., Algeo, T.J., Bottjer, D.J., Yu, J., Xu, G., Penman, D., Wang, Y., Li, L., Shi, X., 2022. Intensified continental chemical weathering and carbon-cycle perturbations linked to volcanism during the Triassic–Jurassic transition. Nat. Commun. 13 (1), 1–10. https://doi.org/10.1038/s41467-022-27965-x.
- Sial, A.N., Lacerda, L.D., Ferreira, V.P., Frei, R., Marquillas, R.A., Barbosa, J.A., Gaucher, C., Windmöller, C.C., Pereira, N.S., 2013. Mercury as a proxy for volcanic activity during extreme environmental turnover: The Cretaceous–Paleogene transition. Palaeogeogra. Palaeoclimatol. Palaeoecol. 387, 153–164. https://doi. org/10.1016/j.palaeo.2013. 07.019.
- Skyllberg, U., Drott, A., 2010. Competition between disordered iron sulfide and natural organic matter associated thiols for mercury (II)-an EXAFS study. Environ. Sci. Technol. 44 (4), 1254–1259. https://doi.org/10.1021/es902091w.
- Sørensen, A.L., Nielsen, A.T., Thibault, N., Zhao, Z., Schovsbo, N.H., Dahl, T.W., 2020. Astronomically forced climate change in the late Cambrian. Earth Planet. Sci. Lett. 548, 116475 https://doi.org/10.1016/j.epsl.2020.116475.
- Sturesson, U.L.F., Popov, L.E., Holmer, L.E., Bassett, M.G., Felitsyn, S., Belyatsky, B., 2005. Neodymium isotopic composition of Cambrian–Ordovician biogenic apatite in the Baltoscandian Basin: implications for palaeogeographical evolution and patterns of biodiversity. Geol. Mag. 142, 419–439. https://doi.org/10.1017/S0016756805000877.
- Sun, R., Enrico, M., Heimbürger, L.E., Scott, C., Sonke, J.E., 2013. A double-stage tube furnace—acid-trapping protocol for the pre-concentration of mercury from solid samples for isotopic analysis. Anal. Bioanal. Chem. 405, 6771–6781. https://doi. org/10.1007/s00216-013-7152-2.
- Thibodeau, A.M., Ritterbush, K., Yager, J.A., West, A.J., Ibarra, Y., Bottjer, D.J., Berelson, W.M., Bergquist, B.A., Corsetti, F.A., 2016. Mercury anomalies and the timing of biotic recovery following the end-Triassic mass extinction. Nat. Commun. 7, 1–8.
- Tsui, M.T.K., Blum, J.D., Kwon, S.Y., 2020. Review of stable mercury isotopes in ecology and biogeochemistry. Sci. Total Environ. 716, 135386 https://doi.org/10.1016/j. scitoteny.2019. 135386.
- Vozárová, A., Šarinová, K., Larionov, A., Presnyakov, S., Sergeev, S., 2010. Late Cambrian/Ordovician magmatic arc type volcanism in the Southern Gemericum basement, Western Carpathians, Slovakia: U–Pb (SHRIMP) data from zircons. Int. J. Earth Sci. 99, 17–37. https://doi.org/10.1007/s00531-009-0454-0.
- Wolfenden, S., Charnock, J.M., Hilton, J., Livens, F.R., Vaughan, D.J., 2005. Sulfide species as a sink for mercury in lake sediments. Environ. Sci. Technol. 39 (17), 6644–6648. https://doi.org/10.1021/es048874z.
- Zambardi, T., Sonke, J.E., Toutain, J.P., Sortino, F., Shinohara, H., 2009. Mercury emissions and stable isotopic compositions at Vulcano Island (Italy). Earth Planet. Sci. Lett. 277 (1–2), 236–243. https://doi.org/10.1016/j.epsl.2008.10.023.
- Zerkle, A.L., Yin, R., Chen, C., Li, X., Izon, G.J., Grasby, S.E., 2020. Anomalous fractionation of mercury isotopes in the late Archean atmosphere. Nat. Commun. 11, 1–9. https://doi.org/10.1038/s41467-020-15495-3.
- Zerkle, A.L., Claire, M., Di Rocco, T., Grassineau, N., Nisbet, E., Sun, R., Yin, R., 2021.
 Sulfur and mercury MIF suggest volcanic contributions to Earth's atmosphere at 2.7
 Ga. Geochem. Perspect. Lett. 18, 48–52. https://doi.org/10.7185/geochemlet.2124.
- Zhang, S.H., Fan, J.X., Morgan, C.A., Henderson, C.M., Shen, S.Z., 2021. Quantifying the middle-late Cambrian trilobite diversity pattern in South China. Palaeogeogr. Palaeoclimatol. Palaeoecol. 570, 110361 https://doi.org/10.1016/j. palaeo.2021.110361.
- Zhao, Z., Ahlberg, P., Thibault, N., Dahl, T.W., Schovsbo, N.H., Nielsen, A.T., 2022. High-resolution carbon isotope chemostratigraphy of the middle Cambrian to lowermost Ordovician in southern Scandinavia: Implications for global correlation. Glob. Planet. Change, 103751. https://doi.org/10.1016/j.gloplacha.2022.103751.
- Zhou, T., Pan, X., Sun, R., Deng, C., Shen, J., Kwon, S.Y., Grasby, S.E., Xiao, J., Yin, R., 2021. Cryogenian interglacial greenhouse driven by enhanced volcanism: evidence from mercury records. Earth Planet. Sci. Lett. 564, 116902 https://doi.org/10.1016/i.epsl.2021.116902.
- Zhu, D.C., Zhao, Z.D., Niu, Y., Dilek, Y., Wang, Q., Ji, W.H., Dong, G.C., Sui, Q.L., Liu, Y. S., Yuan, H.L., Mo, X.X., 2012. Cambrian bimodal volcanism in the Lhasa Terrane, southern Tibet: record of an early Paleozoic Andean-type magmatic arc in the Australian proto-Tethyan margin. Chem. Geol. 328, 290–308. https://doi.org/10.1016/j.chemgeo.2011.12.024.